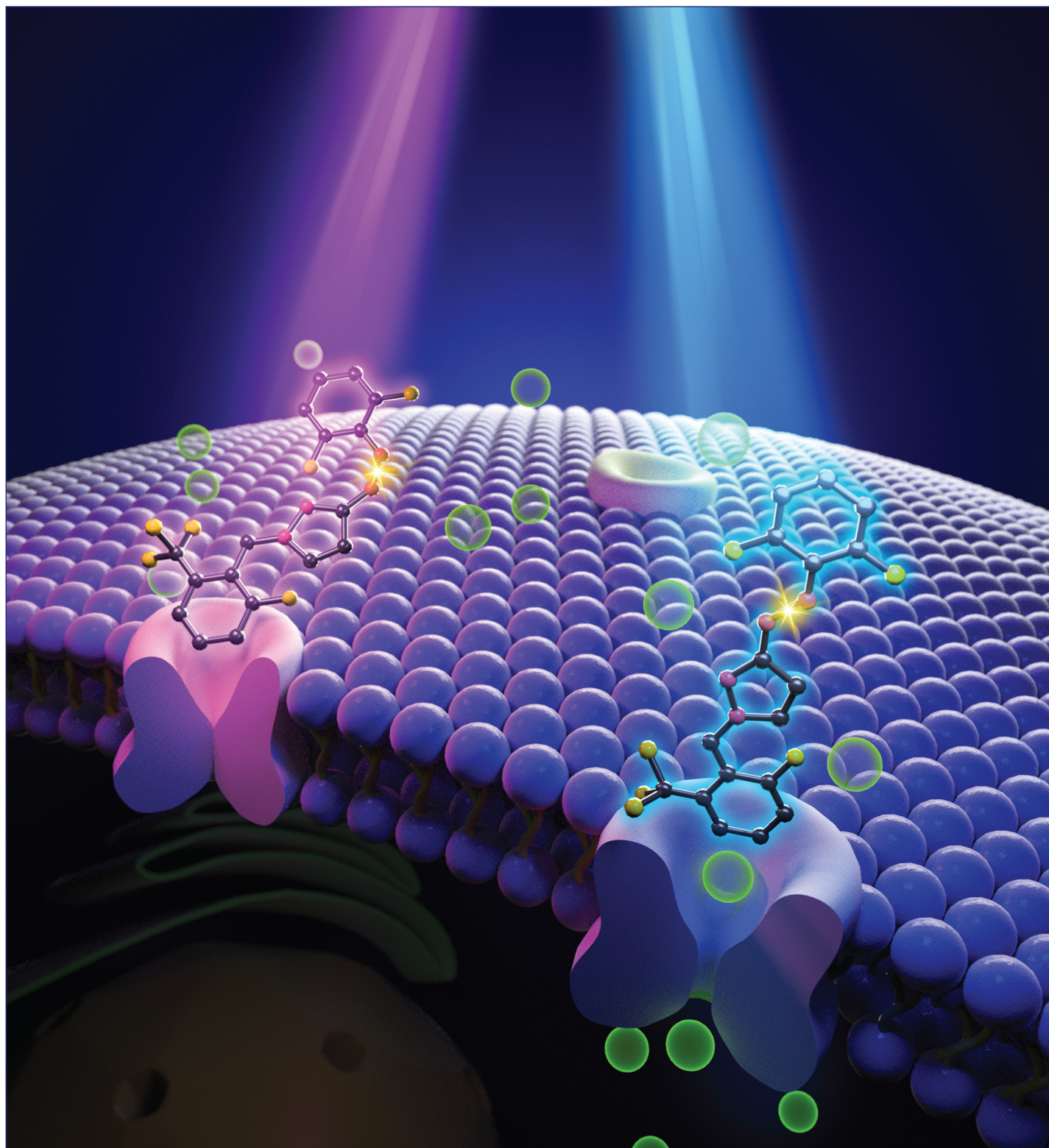


July 1, 2020
Volume 142
Number 26
pubs.acs.org/JACS

J | A | C | S

JOURNAL OF THE AMERICAN CHEMICAL SOCIETY



ACS Publications
Most Trusted. Most Cited. Most Read.

www.acs.org

Optical Control of CRAC Channels Using Photoswitchable Azopyrazoles

Xingye Yang,[⊥] Guolin Ma,[⊥] Sisi Zheng,[⊥] Xiaojun Qin, Xiang Li, Lupei Du, Youjun Wang,^{*} Yubin Zhou,^{*} and Minyong Li^{*}



Cite This: *J. Am. Chem. Soc.* 2020, 142, 9460–9470



Read Online

ACCESS |



Metrics & More

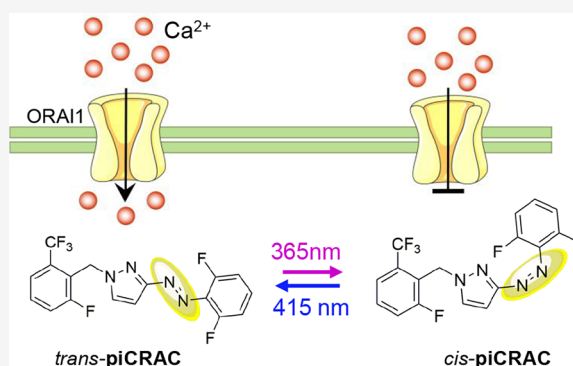


Article Recommendations



Supporting Information

ABSTRACT: The Ca²⁺ release-activated Ca²⁺ (CRAC) channels control many Ca²⁺-modulated physiological processes in mammals. Hyperactivating CRAC channels are known to cause several human diseases, including Stormorken syndrome. Here, we show the design of azopyrazole-derived photoswitchable CRAC channel inhibitors (designated piCRACs), which enable optical inhibition of store-operated Ca²⁺ influx and downstream signaling. Moreover, piCRAC-1 has been applied *in vivo* to alleviate thrombocytopenia and hemorrhage in a zebrafish model of Stormorken syndrome in a light-dependent manner.



INTRODUCTION

The Ca²⁺ release-activated Ca²⁺ (CRAC) channel comprising STIM and ORAI proteins is a prototypical example of a store-operated Ca²⁺ entry (SOCE) and serves as an indispensable highly selective Ca²⁺ entry route in both excitable and nonexcitable cells.^{1–3} SOCE is initiated by Ca²⁺ store depletion within the lumen of the endoplasmic reticulum (ER) and subsequent multimerization of the STIM1 ER-luminal domain.⁴ Activated STIM1 molecules accumulate at ER–PM junctions to engage and directly gate ORAI channels, permitting Ca²⁺ flux into cells.^{5–10} Aberrant STIM–ORAI signaling has been linked to several human diseases, including immunodeficiency, autoimmune-inflammatory disorders, cardiac hypertrophy, cancer metastasis, and the Stormorken syndrome.^{3,11} Stormorken syndrome is believed to arise from gain-of-function mutations in either ORAI1 or STIM1 (e.g., R304W) that lead to constitutive Ca²⁺ entry.^{12,13} Therefore, the CRAC channel has been actively pursued as a promising therapeutic target. Several small molecules targeting CRAC channels have been developed, with some entering clinical trials.^{14–16} Among them, the GSKs series^{17–19} and Synta 66^{20–24} are regarded as relatively specific CRAC channel inhibitors with IC₅₀ values in the range of 1–4 μM.^{17,25} The field still lacks switchable CRAC channel blockers that might cause less systemic side effects.

Optogenetic approaches have been recently employed to modulate Ca²⁺ channels with high spatiotemporal resolution.^{26–28} However, optogenetic manipulation is limited in certain applications because it requires the delivery of exogenous genes and expression of non-native proteins. By

contrast, photopharmacological approaches^{29–32} use photoswitchable molecules to exert precise spatiotemporal control over the action of bioactive targets, such as ion channels,^{33–35} receptors,^{36–38} enzymes,³⁹ and nucleic acids.⁴⁰ To more precisely control CRAC channel activity, we set out to develop a series of photoswitchable inhibitors that allow for optical inhibition of Ca²⁺ signaling with good spatiotemporal resolution, thereby permitting photopharmacological modulations of diseases associated with overactivated CRAC channels, such as Stormorken syndrome. These tools are anticipated to complement the existing genetically encoded optogenetic actuators that allow light-inducible activation of CRAC channels.^{28,41–44}

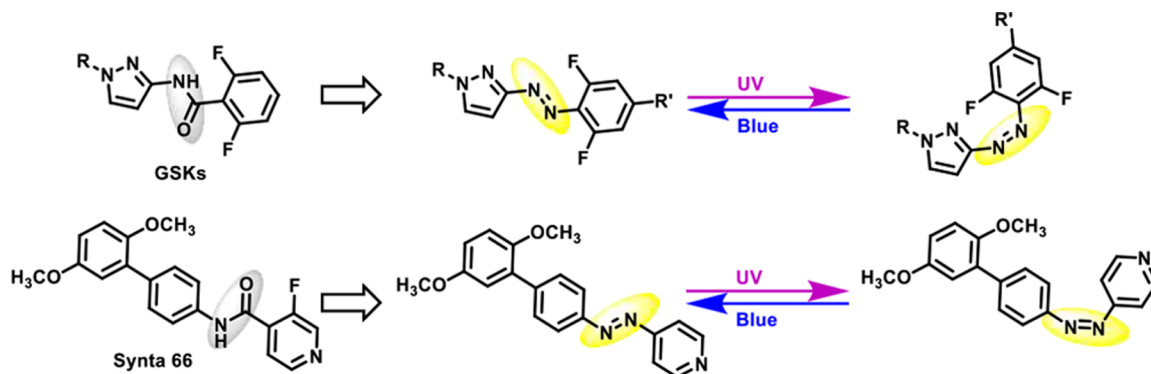
RESULTS AND DISCUSSION

Design, Synthesis, and Characterizations of Photo-Inducible CRAC Channel Inhibitors (Termed as piCRACs). Pyrazole-derived inhibitors of CRAC channels such as the GSK series^{17,18} and Synta 66²⁰ have heterocyclic *N*-aryl benzamide⁴⁵ backbone structures. We resorted to bioisosteric replacement by substituting the amide group of these compounds with azo-group to lend themselves toward azologization for photoconversion.⁴⁵ We envisioned that the

Received: March 16, 2020

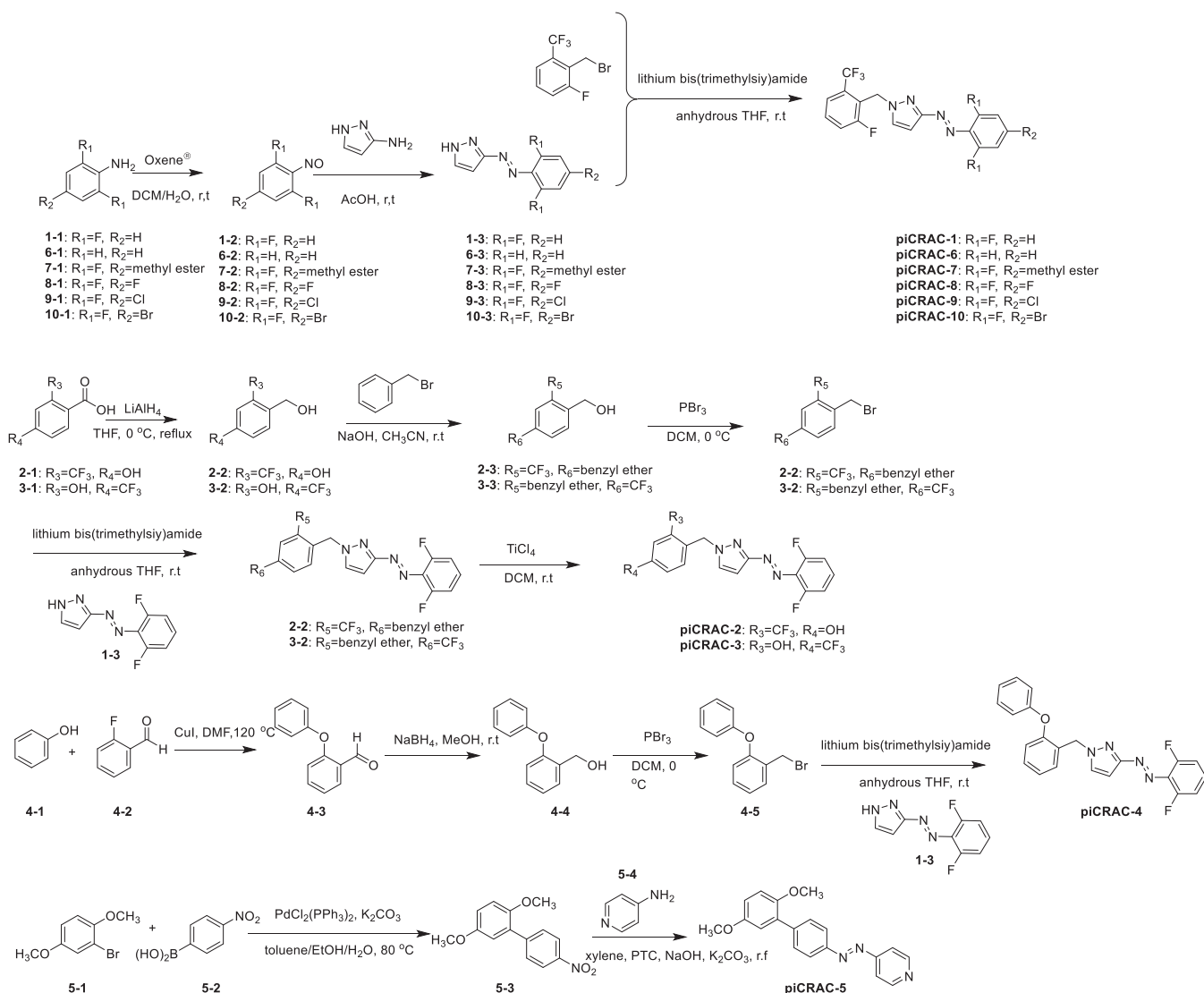
Published: April 24, 2020



Scheme 1. Converting CRAC Channel Inhibitors, GSKs and Synta 66, into Photoswitchable Derivatives, piCRACs^a

^apiCRACs undergo reversible *trans*-to-*cis* isomerization upon illumination with light emitting at different wavelengths. Irradiation in the UV range leads to conversion from the *trans* to *cis* configuration, whereas blue light stimulation switches the *cis* isomer back to a *trans* conformation.

Scheme 2. Synthesis of piCRACs Based on the Prototypic Compounds of Well-Known CRAC Channel Inhibitors GSK-5498A, GSK-7975A, GSK-5503A, and Synta 66



engineered photoswitchable compounds could only inhibit SOCE under one configuration, and the light-induced *trans*-to-*cis* isomerization of the azobenzene moiety would enable light-switchable inhibition on SOCE (Scheme 1 and Figure S1).

Four synthesis routes were developed on the basis of the prototype compounds from well-known CRAC channel inhibitors, including GSK-5498A, GSK-7975A, GSK-5503A, and Synta 66 (Scheme 2 and Figure S1). A series of

nitrosaniline analogues were obtained by aniline oxidation. Azopyrazole analogues were formed by Mills reaction in glacial acetic acid followed by substitution to yield **piCRAC-1**, **-6–10**. **PiCRAC-2** and **-3** were prepared via the reducing benzoic acid, protecting phenol, bromo-substituted benzyl alcohol, substitution, and deprotection reaction. **PiCRAC-4** was produced by following the Ullmann reaction, reduction, bromination, and substitution. With the Suzuki coupling and diazo-coupling reaction, **piCRAC-5** was synthesized.

We then moved on to characterize the photochemical properties of **piCRACs** *in vitro*. To identify the optimal activation window for photoconversion, we measured the absorption spectra of **piCRACs** after irradiation under various wavelengths (Figure 1c and Figure S2a–d). The UV–vis

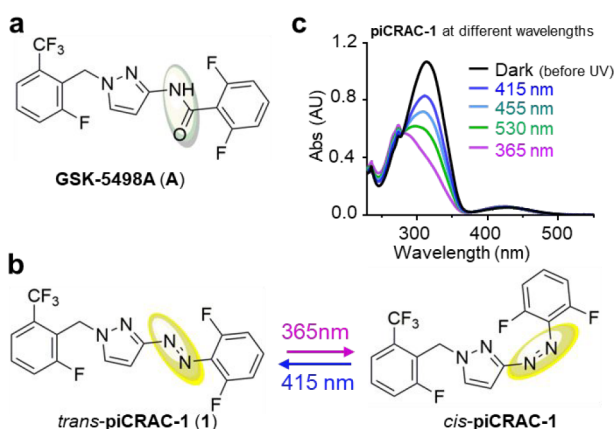


Figure 1. Design and photochemical properties of **piCRAC-1**. (a,b) Chemical structures of **GSK-5498A** (compound **A**) and light-inducible isomerization of its photoswitchable derivative **piCRAC-1** (compound **1**). **PiCRAC-1** undergoes reversible *trans*-to-*cis* isomerization upon illumination with lights emitting at different wavelengths. Irradiation at 365 nm leads to conversion from the *trans* to *cis* configuration, whereas 415 nm light stimulation switches the *cis* isomer back to a *trans* conformation. (c) UV–vis spectra of **piCRAC-1** (50 μ M) at different irradiation wavelengths in acetonitrile containing 0.5% DMSO.

spectra of **piCRAC-1–5** were similar to the signature absorption spectra of azobenzenes with photoconverted characteristics between *trans* (*E*) and *cis* (*Z*) states. The best photoconversions were generally achieved with 365 nm (*E–Z*) and 415 nm (*Z–E*) irradiation (Figure 1c and Figure S2a–d). These wavelengths were thus used in the following experiments.

By using thapsigargin (TG)-induced store-operated calcium entry (SOCE) and Ca^{2+} -dependent nuclear entry of NFAT as two independent readouts, we examined the biological activities of **piCRACs**. We first assessed **piCRACs**' photoresponsiveness and compared their abilities to inhibit CRAC channels under the following conditions: the initially synthesized compounds without any light illumination defined as the "dark" status, which was further exposed to 365 or 415 nm light, respectively. Among the five tested **piCRACs** (1–5, at 10 μ M), **piCRAC-1** (Figure 1) derived from **GSK-5498A** showed the most potent UV-light-inducible suppression of TG-induced SOCE (Figure S3a) and NFAT nuclear translocation (Figure S3b). **PiCRAC-2** and **piCRAC-5** failed to inhibit CRAC channel regardless of UV and blue light stimulation. As compared to **piCRAC-1**, **piCRAC-3** and **piCRAC-4** showed strong background and poor isomerization. Thus, **piCRAC-1** as the lead compound was further characterized and optimized.

We then monitored the relative abundance of the *trans* and *cis* isomers of **piCRAC-1** by HPLC (Table 1). The results showed that all PSS of **piCRAC-1** contained a mixture of both isomers. **PiCRAC-1** mostly existed in a *trans* configuration (>95%) in the dark (Table 1), but contained 49.0% *cis* isomer under 365 nm illumination. To obtain a higher conversion rate, we moved forward to design and synthesize new **GSK-5498A** derivatives **piCRAC-6–10** by removing steric-effect-inducing groups or adding additional para-electron-withdrawing groups to **piCRAC-1**.^{46,47} Consistent with previous reports,^{46,47} these modifications significantly increased photoisomerization rates of **piCRAC-6–10** (Table 1 and Figure S2e–i). However, *in cellulo* functional testing results showed that these new sets of **piCRACs** had no biological activity as they did not inhibit SOCE (Figure S4). We thus focused on **piCRAC-1** and thoroughly tested its photochemical and biological properties.

We further examined the real-time isomerization of **piCRAC-1** by monitoring UV–vis spectra, HPLC, and $^1\text{H}/^{19}\text{F}$ NMR profiles. Prior to 365 nm illumination (at 415 nm or in the dark), **piCRAC-1** primarily adopted a *trans* configuration, as reflected by a strong absorbance peak at 314 nm in the UV–vis spectra (Figure 2a, black trace) and a single peak corresponding to *trans-piCRAC-1* in the HPLC elution profile (Figure 2c, top trace at 0 s). Upon UV irradiation at 365 nm, the *trans-piCRAC-1* was converted into a *cis* state, as characterized by the decrease of absorbance at 314 nm (Figure 2a, violet curves) and a newly emerged secondary peak in the HPLC profile (Figure 2c). After 3–5 min of UV illumination, 49.0% of *trans-piCRAC-1* was switched to the *cis* state on the basis of the HPLC profiles (Figures 2c and S5c and Table 1).

Table 1. Photostationary States (PSS) for **piCRAC-1** and **piCRAC-6–10** at Different Irradiation Wavelengths

compd ^a	R ₁	R ₂	dark (area% <i>cis</i>)	365 nm (area% <i>cis</i>)	415 nm (area% <i>cis</i>)	455 nm (area% <i>cis</i>)	530 nm (area% <i>cis</i>)
piCRAC-1 *	–F	–H	3.7 ± 0.1	49.0 ± 0.3	15.5 ± 0.1	22.9 ± 0.1	33.2 ± 0.1
piCRAC-1 **	–F	–H	4.6 ± 0.2	60.3 ± 0.7	19.8 ± 0.6	25.3 ± 0.4	25.8 ± 0.4
piCRAC-6 *	–H	–H	4.7 ± 0.4	50.4 ± 3.0	12.9 ± 3.5	11.0 ± 0.1	10.7 ± 0.1
piCRAC-7 *	–F	–methyl ester	0	80.3 ± 0.2	18.4 ± 0.1	28.6 ± 0.7	47.5 ± 0.2
piCRAC-8 *	–F	–F	0	52.3 ± 0.5	18.5 ± 1.5	20.0 ± 1.5	26.5 ± 0.1
piCRAC-9 *	–F	–Cl	0.9 ± 0.5	73.1 ± 0.6	22.8 ± 3.9	24.2 ± 0.1	32.8 ± 0.1
piCRAC-10 *	–F	–Br	15.8 ± 3.0	76.9 ± 0.3	19.5 ± 0.1	24.8 ± 0.1	33.6 ± 0.1

^aThe percentages of photostationary state area at dark, 365 nm (9.8 mW), 415 nm (14.4 mW), 455 nm (9.5 mW), and 530 nm (6.8 mW) in acetonitrile containing 0.5% DMSO (50 μ M)* or E3 embryo medium containing 0.1% DMSO (10 μ M)** were determined by HPLC analysis at 302 nm. Data were shown PSS ± SEM.

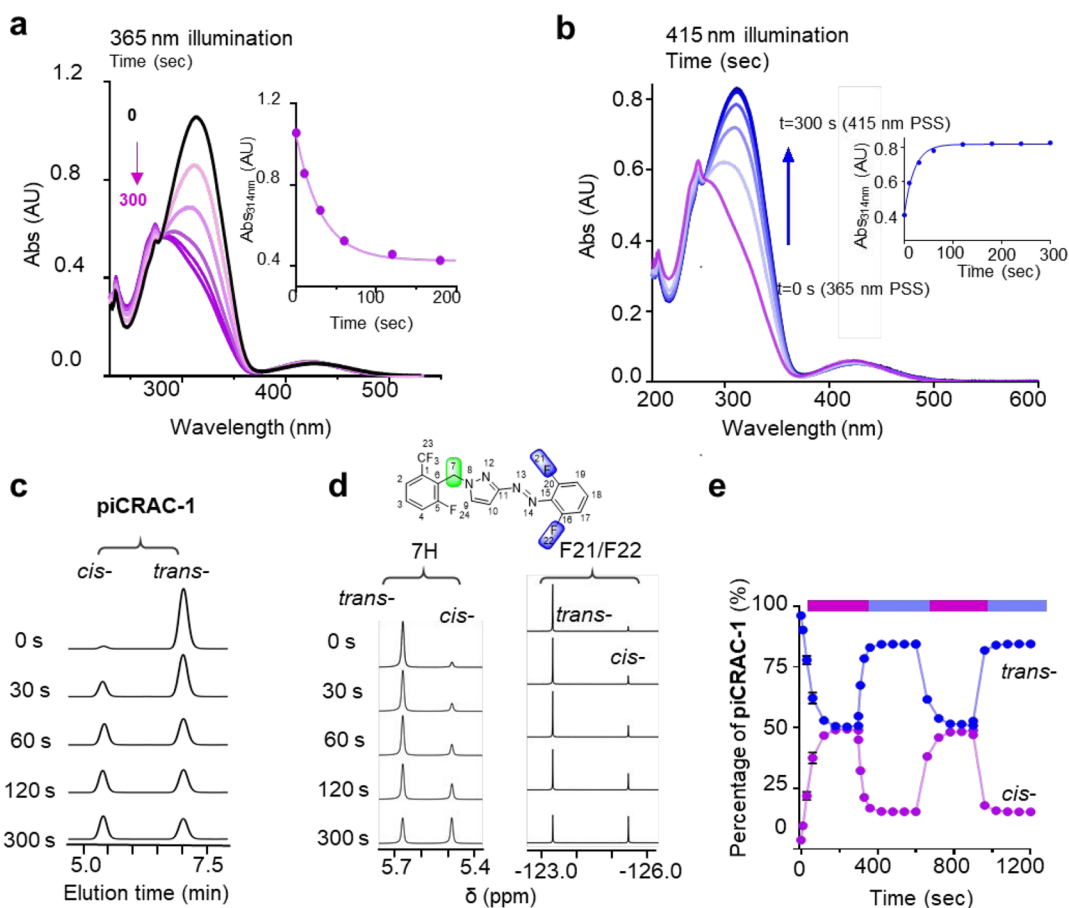


Figure 2. Photochemical properties of **piCRAC-1**. (a,b) Time-resolved UV–vis spectra of **piCRAC-1** (in acetonitrile containing 0.5% DMSO) after illumination at 365 and 415 nm. Inset: Changes of absorbance monitored at 314 nm upon illumination at 365 and 415 nm. (c,d) HPLC elution profiles (c) and selected regions of NMR spectra (d) showing the transition of *trans*-**piCRAC-1** to *cis*-**piCRAC-1** at different UV illumination time points. The representative groups of **piCRAC-1** (35.4 mM) in ^1H NMR and ^{19}F -NMR spectra were indicated in $\text{MeOD-}d_4$. (e) **piCRAC-1** underwent multiple rounds of reversible isomerization with photostability when the illumination between 365 and 415 nm was repeatedly alternated. The *cis* and *trans* isomers of **piCRAC-1** (50 μM) were indicated in acetonitrile containing 0.5% DMSO by the HPLC elution profiles based on (c) and Figure S5c–e ($t_{1/2} = 22.1 \pm 4.2$ s at 365 nm and $t_{1/2} = 14.3 \pm 4.5$ s at 415 nm; error bars are \pm SEM).

A similar trend was visualized by using NMR to monitor the resonance signals of the CH_2 group (H7) adjacent to the pyrazole ring and F21/F22 within the azobenzene group (Figure 2d and Figure S5d). As shown in Figures 2b and S5e,f, *cis* PSS reversed to *trans* PSS upon irradiation at 415 nm. Rapid and reversible photoisomerization was quantified on the basis of HPLC profiles during illuminations at 365 nm (violet trace) or 415 nm (blue trace, Figure 2e), with the photoisomerization half-lives determined to be 22.1 ± 4.2 s at 365 nm and 14.3 ± 4.5 s at 415 nm (Figure 2e). Following exposure to UV light, the half-life of the *cis* isomer of **piCRAC-1** was determined to be 255.9 days, as measured with the method described by Priimagi et al.⁴⁸ at 25 $^\circ\text{C}$ (Figure S6a–d). Furthermore, no appreciable photodegradation was observed after repeated cycles of photoconversions between 365 and 415 nm (Figure S6e,f). These findings establish **piCRAC-1** as a bistable compound with good photochemical characteristics.

Optical Control of CRAC Channel Activities and Downstream Signaling. We next set out to test the light-dependent inhibitory effects of the **piCRAC-1** on the CRAC channel per se and the downstream Ca^{2+} -responsive transcription factor, the nuclear factor of activated T-cells (NFAT), in mammalian cells. We first examined its ability to suppress SOCE in HEK cells stably expressing GEM-GECO, a

genetically encoded ratiometric Ca^{2+} indicator.^{49,50} Newly synthesized **piCRAC-1** had a minimal effect on SOCE at concentrations lower than 50 μM prior to UV illumination ($\text{IC}_{50} = 73.2$ μM ; Figure 3a). However, after 5 min of UV illumination, **piCRAC-1** showed pronounced inhibition on SOCE, with the IC_{50} value plummeting down to the submicromolar range ($\text{IC}_{50} = 0.5$ μM ; Figure 3a). The performance of **piCRAC-1** at 365 nm seemed to be superior over its prototype, **GSK-5498A** ($\text{IC}_{50} = 3.10$ μM ; Figure S7a). Meanwhile, the light-activated **piCRAC-1** and **GSK-5498A** had comparable inhibition rates over SOCE (Figure S7b,c).

In parallel, we examined the effect of **piCRAC-1** on the CRAC channel current (I_{CRAC}) in HEK cells stably coexpressing STIM1 and ORAI1.⁵¹ We found that **piCRAC-1** suppressed I_{CRAC} by up to 80% when exposed to UV light (365 nm) but not under blue light at 415 nm (Figure 3b,c), indicating that *cis*-**piCRAC-1** is a good CRAC channel inhibitor. To evaluate the specificity of **piCRAC-1**, we also examined its effects on three other major types of Ca^{2+} channels. The results showed that **piCRAC-1** did not inhibit Ca^{2+} responses mediated by $\text{Ca}_v1.2$, TRPC3, and IP_3Rs channels at a concentration that could inhibit SOCE by 86% (10 μM) (Figure S7f–h). Therefore, similar to its prototype **GSK-5498A**, *cis*-**piCRAC-1** is a specific inhibitor of CRAC

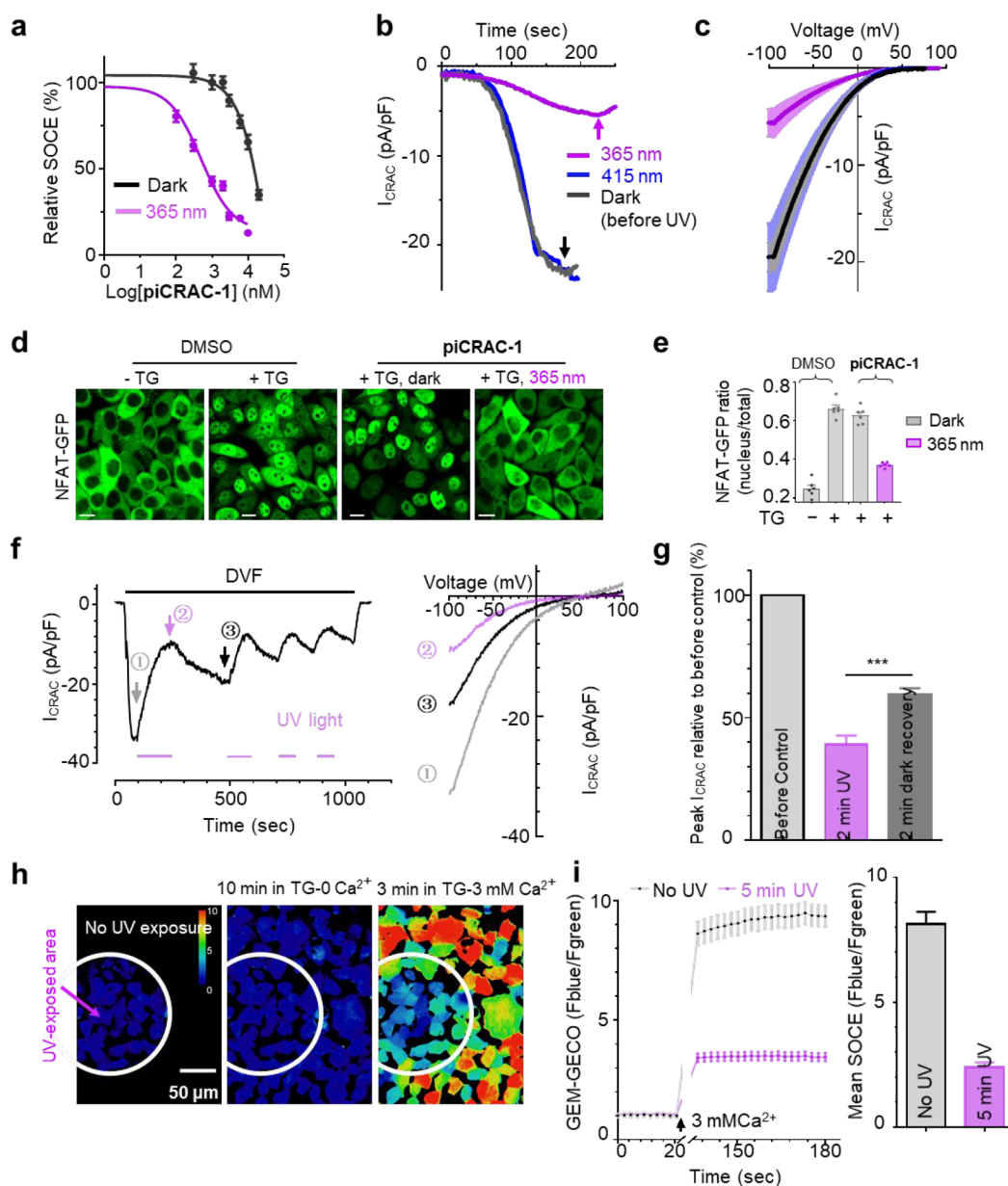


Figure 3. Optical control of CRAC channel and downstream signaling using piCRAC-1. (a) Dose-dependent effects of piCRAC-1 on SOCE in HEK293 GEM-GECO cells before (black curve; IC_{50} : 73.2 μ M) and after 365 nm light stimulation (purple curve; IC_{50} : 0.5 μ M). (b) Representative time courses of normalized inward CRAC channel currents (I_{CRAC} , pA/pF), measured at -100 mV in HEK 293 STIM1-ORAI1 stable cells bathed with 10 μ M piCRAC-1. Cells were kept in the dark prior to light stimulation (dark) and illuminated at either 365 nm (violet) or 415 nm (blue), respectively. Whole-cell I_{CRAC} currents were greatly inhibited after 4 min of UV illumination ($n \geq 6$, -16.1 ± 1.4 pA/pF vs -3.4 ± 1.3 pA/pF). (c) I - V relationships at the peak of I_{CRAC} indicated by arrows in (b). (d) Representative confocal images of HeLa cells stably expressing NFAT1-GFP after treatment with DMSO (control) or piCRAC-1 (10 μ M) in the dark (prior to UV light) or with 365 nm illumination. One micromolar TG was used to trigger Ca^{2+} influx with subsequent NFAT nuclear translocation. Scale bar, 10 μ m. Experiments were repeated three times; 60–100 cells were measured in one image. (e) Quantification of the inhibitory activity of 10 μ M piCRAC-1 against TG-induced NFAT nuclear entry. The ratio of nuclear GFP signals over the whole-cell signals was used as readout. $n = 6$, with 50–100 cells measured for each condition. (f) Typical whole-cell currents of HEK293 cells expressing ORAI1-SS-GFP bathed in DVF solution containing 5 μ M piCRAC-1 (left panel); I - V relationships measured at different time points indicated by arrows (right panel). (g) Statistics from cells shown in panel f (***, $P < 0.0005$, paired Student's t test, $n = 6$). (h) Typical cellular images showing spatial control of SOCE by piCRAC-1. Left panel, one imaging field showing the UV-exposed area (within the white circle) and the non-UV region (the rest of the image). Middle panel, resting cellular GEM-GECO ratios. Left panel, cellular GEM-GECO ratios at the peak of SOCE responses. (i) Time traces (left) and statistics (right) from cells shown in panel h. Data were shown as mean \pm SEM.

channels. We next examined the light-induced effects on the downstream effector NFAT by monitoring its subcellular localization with confocal microscopy. Sarcoplasmic/endoplasmic reticulum Ca^{2+} ATPase inhibitor TG was used as a passive store depletion inducer to trigger SOCE and subsequent

nuclear translocation of NFAT. Upon exposure to UV light, TG-induced NFAT nuclear accumulation was significantly suppressed (Figure 3d,e and Figure S8). Although to a less extent, piCRAC-3 and piCRAC-4 also exhibited a similar

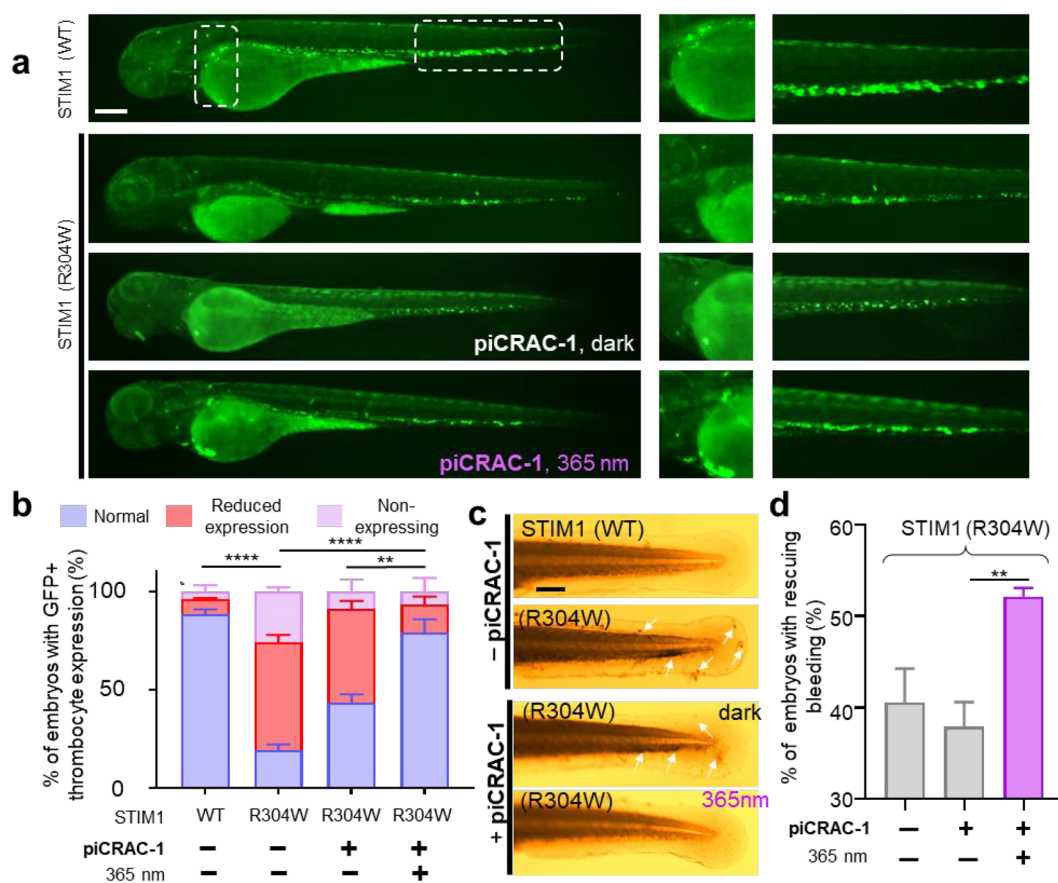


Figure 4. Optical control of piCRAC-1 attenuates Stormorken syndrome-like pathological conditions in zebrafish embryos. (a) Whole-body lateral views of Tg (CD41:EGFP) embryos expressing wild-type (WT) STIM1 or the activating mutant R304W in the absence or presence of 5 μ M piCRAC-1. The embryos were either shielded from UV light prior to photostimulation (dark) or exposed to 365 nm light stimulation for 5 min. Boxed areas with overt changes in thrombocyte progenitors were enlarged and shown on the right. Scale bar, 200 μ m. (b) Quantification of the GFP signals representing thrombocyte progenitors in (a). Three independent experiments were performed, with 25–78 embryos per experiment. Data were shown as mean \pm SEM (** P < 0.01, **** P < 0.0001, two-tailed unpaired Student's t -test). (c,d) Representative images showing *o*-dianisidine staining of embryos expressing WT, STIM1_{WT}, or STIM1_{R304W} (c). The embryos were bathed in the presence of 10 μ M piCRAC-1, either kept in the dark or exposed to UV light (365 nm; 5 min). Quantification of the degrees of hemorrhage was shown on the bar graph (d). Four independent experiments were performed, with 25–75 embryos per experiment. Data were shown as mean \pm SEM (** P < 0.01, two-tailed unpaired Student's t -test).

photoswitchable inhibitory effect on SOCE and nuclear translocation of NFAT (Figure S8).

We next exploited the use of piCRAC-1 for spatial and temporal control of SOCE or CRAC channel activity in HEK293 cells. Ca^{2+} imaging results showed that the UV light-induced suppressive effect on SOCE could be partially reversed after blue light illumination for 15 min (Figure S7d). In 15 min, SOCE responses of piCRAC-1 treated cells recovered by 57%, an extent significantly larger than those of GSK-5498A treated cells after washing out the residual compound (30%) (Figure S7d vs e). Thus, the reversibility of piCRAC-1 seemed to be improved from its mother compound. Further results from whole-cell patch-clamping confirmed that the inhibitory effect of piCRAC-1 was at least partially reversible (Figure 3f,g). We further examined the photoswitchable inhibitory potential of piCRAC-1 on I_{CRAC} with pulses of UV light. UV irradiation inhibited I_{CRAC} in HEK293 cells (Figure 3f). Upon the UV light withdrawal, the amplitudes of I_{CRAC} gradually increased, indicating partial recovery from *cis*-piCRAC inhibition (Figure 3g). This cycle of UV-induced inhibition and dark recovery of I_{CRAC} could be repeated multiple times (Figure 3f), suggesting that the biological activity of piCRAC-

1 could be controlled temporally with partial reversibility. To explore spatial control of SOCE with piCRAC-1, we monitored SOCE responses of HEK293 cells bathed in piCRAC-1 after exposures to locally applied UV flashes. We found that, under the same imaging field, only cells exposed to locally applied UV light showed marked reduction in SOCE (Figure 3h,i). Therefore, piCRAC-1 indeed enabled spatial control of SOCE responses. Together, these data firmly established piCRAC-1 as a photoswitchable CRAC channel blocker at the cellular level.

Optical Control of Stormorken Syndrome in the Zebrafish Model. Moving toward *in vivo* applications, we further investigated whether piCRAC-1 could be used as a noninvasive optical tool to treat CRAC-related channelopathies in the zebrafish model of Stormorken syndrome,^{13,52} which was generated by overexpressing a STIM1 mutant (R304W) to cause constitutive activation of CRAC channels.¹³ The resulting zebrafish embryos have been reported to exhibit Stormorken syndrome-like pathological conditions, including thrombocytopenia and bleeding.¹³ We injected STIM1_{R304W} mRNA into the Tg (CD41:EGFP) line with mature thrombocytes (equivalent of human platelets) and

hematopoietic stem and progenitor cells labeled by GFP⁵³ to monitor their expression levels in developing embryos (Figure 4a,b and Figure S9a,b). As anticipated, embryos expressing STIM1_R304W showed a significant reduction in GFP signals in the tails that were indicative of thrombocytopenia, as well as overt hemorrhage in the tail as revealed by *o*-dianisidine staining of hemoglobin (Figure 4c,d). After ensuring that the protein levels of expressed STIM1_R304W were similar among all experimental groups (Figure S10), we treated 3 dpf (day 3 postfertilization) zebrafish embryos with 5 μ M piCRAC-1 with and without exposure to UV or blue light. We found that 365 nm-excited piCRAC-1 markedly rescued thrombocytopenia, as indicated by significantly enhanced GFP signals emitting from mature thrombocytes ($78.9 \pm 6.9\%$; Figure 4a,b). By contrast, embryos incubated with piCRAC-1 without 365 nm illumination or under 415 nm light stimulation failed to effectively rescue thrombocytopenia (Figure S9b). Interestingly, we noticed that dark PSS and 415 nm PSS of piCRAC-1 rescued thrombocytopenia slightly, probably due to incomplete light-induced conversion of *cis*-piCRAC-1. Most importantly, piCRAC-1 effectively ameliorated the abnormal bleeding at the tail exposed to brief UV light illumination (Figure 4c,d).

Taken together, these results indicated that piCRAC-1 could serve as a phototunable agent to alleviate pathological conditions associated with hyperactive CRAC channel activities, such as Stormorken syndrome.

CONCLUSIONS

In summary, we developed a series of photoswitchable CRAC channel modulators named as piCRACs through bioisosteric replacement in heterocyclic *N*-aryl benzamide-derived SOCE inhibitors. The introduction of azoster moiety into these compounds enables rapid and reversible photoconversion between the *trans* and *cis* configurations, thereby allowing piCRACs to exhibit contrasting inhibitory effects on the CRAC channels (with IC₅₀ values varying by ~150-fold for piCRAC-1 in the dark vs 365 nm). Among them, the bistable piCRAC-1 effectively inhibits SOCE or I_{CRAC} in a light-dependent manner, with the affinity and kinetics comparable to the unmodified prototype GSK-5498A. PiCRAC-1 permits light-inducible modulation of both CRAC channels and Ca²⁺-dependent physiological processes *in cellulo* with appropriate spatiotemporal precision. Most excitingly, we have successfully demonstrated the use of piCRAC-1 as a potential therapeutic agent to optically intervene in pathological conditions associated with dysregulated Ca²⁺ signaling, such as Stormorken syndrome arising from overactivating mutations of CRAC channels.^{13,52}

The majority of azologues seem to be more bioactive in their *trans*-form,^{45,54} but *cis*-active photoswitches are equally appealing as they are inactive in the dark state and can be conveniently activated with light. PiCRAC-1 takes action in its *cis*-configuration, making it a new addition to the *cis*-on photopharmacology toolbox. We anticipate that this chemical biology toolkit may not only facilitate the study of structure–function relations of Ca²⁺ channels but also has the potential to interrogate a myriad of Ca²⁺-regulated signaling events and human disorders associated with imbalanced Ca²⁺ homeostasis.^{1–3,11}

EXPERIMENTAL SECTION

Chemical Synthesis. Compounds were chemically synthesized by following the general procedures,^{55,56} including modifications (synthetic routes are shown in the Supporting Information). All reagents and solvents were purchased from commercial sources (Meryer, Aladdin, J&K Chemical, Energy Chemical, and Heowns Inc.) and were used without further purification unless otherwise noted. Dry tetrahydrofuran (THF) was distilled from Na/benzophenone before use. All reactions were monitored by TLC on glass coated with silica gel 60F254 (0.2 mm thickness) and visualized by UV irradiation at 254 nm. Column chromatography was performed using silica gel (SiO₂, 200–300 mesh, Haiyang Chem). The preparation methods were described in the synthesis in the Supporting Information.

Photochemical Characteristics. UV–vis spectra were recorded using TU-1901 and TU-1905 (PERSEE) with 10 mm light path cuvettes. All piCRAC compounds were dissolved at a concentration of 50 μ M in acetonitrile containing 0.5% DMSO. PiCRAC-1 was dissolved at a concentration of 10 μ M in E3 embryo medium (5 mM NaCl, 0.17 mM KCl, 10 mM HEPES, 0.33 mM MgSO₄, 0.33 mM CaCl₂) containing 0.1% DMSO. The cuvettes were directly irradiated by a fiber-coupled LED (Thorlabs). An initial spectrum was obtained for each newly synthesized compound (defined as dark PSS). Illumination at 365 nm was used to initiate the π – π^* transition for *trans*-to-*cis* isomerization.⁵⁷ The 415, 455, and 530 nm LED were further used to illuminate the sample during UV–vis spectra acquisition. Time-resolved UV–vis spectra of compounds were recorded at the same conditions by monitoring the absorbance at a fixed wavelength at different time points.

The ¹H, ¹⁹F, and ¹³C NMR spectra were respectively obtained on a Bruker Avance AVIII-400 spectrometer at 400 (¹H), 376 (¹⁹F), and 101 MHz (¹³C). CDCl₃, MeOD-*d*₄, and DMSO-*d*₆ (CIL, Energy Chemical) were used as the solvents. δ H, δ F, and δ C were expressed in parts per million (ppm, δ scale). The ¹H and ¹⁹F NMR spectra of 35.4 mM of piCRAC-1 in MeOD-*d*₄ were acquired by illuminating the sample at 365 or 415 nm at the indicated time points. The changes in spectra were measured at each time point. NMR spectra were displayed below. HR-ESI–MS was performed by using an Agilent 6510 Q-TOF mass spectrometer. ESI–MS spectra were obtained by using a Thermo Fisher CQ Fleet instrument.

Cell Culture. HEK 293 or HEK 293 cells stably expressing GEM-GECO (Addgene; #32442) or ORAI1/STIM1 were used as described previously.^{51,58,59} HEK cells were cultured in DMEM (HyClone) supplemented with 10% FBS (Gemini Bio-Products), 5% penicillin, and streptomycin (Thermo Scientific) at 37 °C with 5% CO₂.⁵⁸ The GEM-GECO stable cell line was made as previously described^{58,59} and was maintained in the presence of 2 μ g/mL puromycin (Gibco).

Intracellular Ca²⁺ Imaging. Cytosolic Ca²⁺ was conducted using a ZEISS Observer-Z1 imaging system controlled with Zen2 software.^{58,59} All filters or filter sets were purchased from Semrock (BrightLine). Ca²⁺ signals indicated by GEM-GECO fluorescence were acquired using a customized GEM filter set purchased from Semrock. Fluorescence signals were acquired with a rate of one frame per 2 s by setting the excitation at 387 ± 12 nm and the emission at 549 ± 21 nm (F_{Green}) and 465 ± 32 nm (F_{Blue}). The cytosolic Ca²⁺ level was presented as the ratio of $F_{\text{Blue}}/F_{\text{Green}}$.⁵¹ The imaging solution consisted of 107 mM NaCl, 7.2 mM KCl, 1.2 mM MgCl₂, 11.5 mM glucose, and 20 mM HEPES-NaOH at pH 7.2. A UV light was used as the external source for photostimulation.²⁷ For assays to demonstrate the spatial control of piCRAC-1 on SOCE, localized UV light was applied to store-depleted cells in the center of the view-field by setting the aperture for excitation light to a minimum and keeping UV light on for 2 min. Representative traces from at least three independent experiments were shown as mean \pm SEM as we did previously.^{51,58,60}

Electrophysiological Measurements. Whole-cell recordings were performed using HEK STIM1-ORAI1 dual-expression stable cells as described previously.⁵¹ Briefly, currents were recorded using an EPC-10 (HEKA Elektronik) at room temperature. The membrane potential was held at 0 mV, and 50 ms voltage ramps ranging from

–100 to 100 mV were delivered every 2 s. A 10 mV junction potential compensation was applied to correct the liquid junction potential of the pipet solution relative to the extracellular solution. The intracellular or pipet solution contained 135 mM Cs-aspartate, 8 mM MgCl₂, 10 mM EGTA, and 10 mM Cs-HEPES (pH 7.2), with the osmotic pressure set at 320 ± 3 mOSM/L. The standard extracellular solution contained the following (mM): 115 NaCl, 10 CaCl₂, 10 TEA, 4.5 KCl, and 5 HEPES, and 10 glucose (pH = 7.4, adjusted with NaOH; osmotic pressure = 310 ± 3 mOSM/L). The osmotic pressure of the solution was measured by a freezing point osmometer (OM807, Loser). UV or blue light remained on during the entire recording. To examine the reversibility of piCRAC-1, divalent free (DVF) solution (mM) was used: 150 NaCl, 10 EDTA, 10 TEA, and 5 HEPES, and 10 glucose (pH = 7.4, adjusted with NaOH; osmotic pressure ~307 mOSM/L).⁶¹ The compounds were added to the standard extracellular solution. After stabilization of the whole-cell current, cycles of UV (365 nm) illumination were applied with various intervals. The HEKA Fitmaster and Matlab 2014b software packages were used for offline data analysis. Data were presented from at least six individual cells for each condition.

Fluorescence Imaging. HeLa cells stably expressing NFAT1(1-460)-GFP were seeded in a black glass-bottom 96-well microplate with 3000 cells/well and were cultured in 40 μL of Dulbecco's modified eagle's medium (DMEM) supplemented with 10% FBS in 5% CO₂ at 37 °C. Six hours after culture, the old media were replaced by fresh media containing 10 μM compound (diluted from 5 mM stock dissolved in DMSO). Each compound was added individually to six wells, which were subdivided into two groups: UV and dark. The dark group was shielded from light stimulation by sealing the wells with aluminum foil. The UV group was illuminated by UV light at 365 nm for 10 min. One micromolar TG was subsequently added to both groups, with the mixture incubated for 20 min in the dark or lit conditions, respectively. Next, the plate was washed with PBS twice, and the cells were fixed with 4% PFA for 15 min at room temperature and then treated with 0.1% Triton X-100 for 10 min. The cells were subsequently stained with DAPI (1 mg/mL) for 2 min, followed by washing with PBS twice prior to imaging.

Fluorescence imaging was performed on a Nikon Eclipse Ti-E microscope (Nikon) equipped with an A1R-A1 confocal module with LU-N4 laser sources (argon ion: 405 and 488 nm) and a CFI (chrome-free infinity) plan Achromat VC series objective lens (40×). Each well was captured for four fields with a built-in automated sampling module. The confocal images were analyzed by the NIS-Elements AR microscope imaging software (Nikon, NIS-element AR version 4.5). The cytosolic and nuclear intensities of NFAT1-GFP signals were statistically analyzed by a semiautomatic image analysis tool of the NIS-element AR software. The collected data were further plotted by the GraphPad Prism software.

Zebrafish Experiments. Adult zebrafish were mated according to standard procedures, and zebrafish embryos were maintained in E3 embryo medium (5 mM NaCl, 0.17 mM KCl, 10 mM HEPES, 0.33 mM MgSO₄, 0.33 mM CaCl₂, 60 mg/L penicillin G sodium salt, and 100 mg/L streptomycin sulfate; pH 7.8). To generate capped human mRNA, the cDNAs encoding STIM1_WT (NM_003156) and STIM1_R304W were first inserted into a pCS2+ vector by using the Gateway cloning technology, followed by linearization with EcoRI digestion. Capped mRNAs were prepared by using the mMACHINE mMACHINE SP6 Transcription Kit (Invitrogen). Capped mRNAs were dissolved in PBS and microinjected into fertilized eggs at 100 pg/embryo. Embryos were maintained in 0.2 mM 1-phenyl-2-thiourea (Aladdin) to prevent pigment formation. The Tg (CD41:EGFP) line⁵³ was obtained from the China Zebrafish Resource Center. The developing embryos were kept at least 3 dpf. Embryos were then treated with DMSO (control), piCRAC-1 (in *trans*- or *cis*-configurations), and GSK-5498A at 5 μM for 2.5 h.

To quantify the number of cells with high levels of GFP signals, Tg(CD41:EGFP) embryos were anesthetized with 0.016% tricaine (Bide Pharm) and mounted on a glass culture dish coated with 3% agarose (BioFr). Images were acquired using an OLYMPUS SZX16 microscope equipped with an AxioCam MRm CCD camera and a

light source for EGFP excitation (488 nm). Images were processed by using the ImageJ software (NIH). The data were plotted with the GraphPad Prism software.

For spontaneous bleeding, embryos were stained with 0.6 mg/mL *o*-dianisidine (J&K Chemical), 0.01 M NaOAc (pH 4.6), 0.65% H₂O₂, and 40% (v/v) EtOH in the dark for 15 min. Stained embryos were washed with 1% PBST three times. Freshly prepared 4% paraformaldehyde was used fixed at room temperature for 30 min and then scored for bleeding phenotype.

Western Blot. The method of embryos culture was the same as described above. Ten eggs were incubated with a RIPA solution containing 100× protease inhibitor and 1 mM PMSF. After homogenization for 1 min, samples were centrifuged at 9000g for 15 min with the supernatant and collected. The total protein content in the supernatant was determined by the bicinchoninic acid assay. Next, an equal volume of loading buffer was added, with the mixture boiled for 4 min for denaturation. The samples were resolved on a 10% SDS-polyacrylamide gel and blotted onto a PVDF membrane blocked with 5% BSA in TBST. Immunodetection was carried out using a rabbit anti-STIM1 antibody (Abcam, 1/2000) or an anti-β-actin (Abcam, 1:2000) as primary antibodies and HRP conjugated Affinipure Goat anti-Rabbit as secondary antibody (Proteintech, 1:4000). Immunoblot detection was carried out using the Lumi-Light chemiluminescence reagent (ThermoFisher) and ChemiScope6000 (Clinx). The intensities of all bands were normalized to β-actin signals (three independent experiments).

All animal studies were approved by the Ethics Committee and IACUC of Cheeloo College of Medicine, Shandong University, and were conducted in compliance with guidelines for the care and use of laboratory animals.

Statistical Analysis. Unless stated otherwise, all data in the present study were presented as mean ± SEM. All *P* values in the studies were determined with a two-tailed, unpaired Student's *t*-test.

Data Availability. All data generated or analyzed during this study are included in this Article (and its Supporting Information) or are available from the corresponding authors upon reasonable request.

■ ASSOCIATED CONTENT

Supporting Information

The Supporting Information is available free of charge at <https://pubs.acs.org/doi/10.1021/jacs.0c02949>.

Detailed synthetic procedures, spectra, and additional data (PDF)

■ AUTHOR INFORMATION

Corresponding Authors

Yubin Zhou – Center for Translational Cancer Research, Institute of Biosciences and Technology, Texas A&M University, Houston, Texas 77030, United States; orcid.org/0000-0001-7962-0517; Email: yubinzhou@tamu.edu

Youjun Wang – Beijing Key Laboratory of Gene Resource and Molecular Development, College of Life Sciences, Beijing Normal University, Beijing 100875, China; Email: wyoujun@bnu.edu.cn

Minyong Li – Department of Medicinal Chemistry, Key Laboratory of Chemical Biology, School of Pharmacy, Cheeloo College of Medicine and Helmholtz International Lab, State Key Laboratory of Microbial Technology, Cheeloo College of Medicine, Shandong University, Jinan, Shandong 250012, China; orcid.org/0000-0003-3276-4921; Email: mli@sdu.edu.cn

Authors

Xingye Yang – Department of Medicinal Chemistry, Key Laboratory of Chemical Biology, School of Pharmacy, Cheeloo

College of Medicine, Shandong University, Jinan, Shandong 250012, China

Guolin Ma – Center for Translational Cancer Research, Institute of Biosciences and Technology, Texas A&M University, Houston, Texas 77030, United States

Sisi Zheng – Beijing Key Laboratory of Gene Resource and Molecular Development, College of Life Sciences, Beijing Normal University, Beijing 100875, China

Xiaojun Qin – Department of Medicinal Chemistry, Key Laboratory of Chemical Biology, School of Pharmacy, Cheeloo College of Medicine, Shandong University, Jinan, Shandong 250012, China

Xiang Li – Department of Medicinal Chemistry, Key Laboratory of Chemical Biology, School of Pharmacy, Cheeloo College of Medicine, Shandong University, Jinan, Shandong 250012, China; orcid.org/0000-0002-7740-1713

Lupei Du – Department of Medicinal Chemistry, Key Laboratory of Chemical Biology, School of Pharmacy, Cheeloo College of Medicine, Shandong University, Jinan, Shandong 250012, China; orcid.org/0000-0003-0531-8985

Complete contact information is available at:
<https://pubs.acs.org/10.1021/jacs.0c02949>

Author Contributions

¹X.Y., G.M., and S.Z. contributed equally.

Notes

The authors declare no competing financial interest.

ACKNOWLEDGMENTS

This work was supported by grants from the National Natural Science Foundation of China (81673393, 91954205, 81874308, and 31671492), the Taishan Scholar Program at Shandong Province, the Qilu Scholar Program at Shandong University, the Shandong Natural Science Foundation (ZR2018ZC0233), the Key Research and Development Project of Shandong Province (2017CXGC1401), the Welch Foundation (BE-1913-20190330), and the American Cancer Society (RSG-16-215-01-TBE).

REFERENCES

- (1) Hogan, P. G.; Lewis, R. S.; Rao, A. Molecular basis of calcium signaling in lymphocytes: STIM and ORAI. *Annu. Rev. Immunol.* **2010**, *28*, 491–533.
- (2) Prakriya, M.; Lewis, R. S. Store-Operated Calcium Channels. *Physiol. Rev.* **2015**, *95* (4), 1383–1436.
- (3) Nguyen, N. T.; Han, W.; Cao, W. M.; Wang, Y.; Wen, S.; Huang, Y.; Li, M.; Du, L.; Zhou, Y. Store-Operated Calcium Entry Mediated by ORAI and STIM. *Compr. Physiol.* **2018**, *8* (3), 981–1002.
- (4) Stathopoulos, P. B.; Zheng, L.; Li, G. Y.; Plevin, M. J.; Ikura, M. Structural and mechanistic insights into STIM1-mediated initiation of store-operated calcium entry. *Cell* **2008**, *135* (1), 110–122.
- (5) Luik, R. M.; Wang, B.; Prakriya, M.; Wu, M. M.; Lewis, R. S. Oligomerization of STIM1 couples ER calcium depletion to CRAC channel activation. *Nature* **2008**, *454* (7203), 538–542.
- (6) Zhang, S. L.; Yu, Y.; Roos, J.; Kozak, J. A.; Deerinck, T. J.; Ellisman, M. H.; Stauderman, K. A.; Cahalan, M. D. STIM1 is a Ca²⁺ sensor that activates CRAC channels and migrates from the Ca²⁺ store to the plasma membrane. *Nature* **2005**, *437* (7060), 902–905.
- (7) Ma, G.; Wei, M.; He, L.; Liu, C.; Wu, B.; Zhang, S. L.; Jing, J.; Liang, X.; Senes, A.; Tan, P.; Li, S.; Sun, A.; Bi, Y.; Zhong, L.; Si, H.; Shen, Y.; Li, M.; Lee, M. S.; Zhou, W.; Wang, J.; Wang, Y.; Zhou, Y. Inside-out Ca(2+) signalling prompted by STIM1 conformational switch. *Nat. Commun.* **2015**, *6*, 7826.

(8) Yuan, J. P.; Zeng, W.; Dorwart, M. R.; Choi, Y. J.; Worley, P. F.; Muallem, S. SOAR and the polybasic STIM1 domains gate and regulate Orai channels. *Nat. Cell Biol.* **2009**, *11* (3), 337–343.

(9) Park, C. Y.; Hoover, P. J.; Mullins, F. M.; Bachhawat, P.; Covington, E. D.; Raunser, S.; Walz, T.; Garcia, K. C.; Dolmetsch, R. E.; Lewis, R. S. STIM1 clusters and activates CRAC channels via direct binding of a cytosolic domain to Orai1. *Cell* **2009**, *136* (5), 876–890.

(10) Muik, M.; Fahrner, M.; Derler, I.; Schindl, R.; Bergsmann, J.; Frischauf, I.; Groschner, K.; Romanin, C. A Cytosolic Homomerization and a Modulatory Domain within STIM1 C Terminus Determine Coupling to ORAI1 Channels. *J. Biol. Chem.* **2009**, *284* (13), 8421–8426.

(11) Lacruz, R. S.; Feske, S. Diseases caused by mutations in ORAI1 and STIM1. *Ann. N. Y. Acad. Sci.* **2015**, *1356*, 45–79.

(12) Morin, G.; Bruechle, N. O.; Singh, A. R.; Knopp, C.; Jedraszak, G.; Elbracht, M.; Bremond-Gignac, D.; Hartmann, K.; Sevestre, H.; Deutz, P.; Herent, D.; Nurnberg, P.; Romeo, B.; Konrad, K.; Mathieu-Dramard, M.; Oldenburg, J.; Bourges-Petit, E.; Shen, Y.; Zerres, K.; Ouadid-Ahidouch, H.; Rochette, J. Gain-of-Function Mutation in STIM1 (P.R304W) Is Associated with Stormorken Syndrome. *Hum. Mutat.* **2014**, *35* (10), 1221–1232.

(13) Nesin, V.; Wiley, G.; Kousi, M.; Ong, E. C.; Lehmann, T.; Nicholl, D. J.; Suri, M.; Shahrizaila, N.; Katsanis, N.; Gaffney, P. M.; Wierenga, K. J.; Tsiokas, L. Activating mutations in STIM1 and ORAI1 cause overlapping syndromes of tubular myopathy and congenital myosis. *Proc. Natl. Acad. Sci. U. S. A.* **2014**, *111* (11), 4197–4202.

(14) Liu, Z.; Li, H.; He, L.; Xiang, Y.; Tian, C.; Li, C.; Tan, P.; Jing, J.; Tian, Y.; Du, L.; Huang, Y.; Han, L.; Li, M.; Zhou, Y. Discovery of Small-Molecule Inhibitors of the HSP90-Calcineurin-NFAT Pathway against Glioblastoma. *Cell chemical biology.* **2019**, *26* (3), 352–365.

(15) Waldron, R. T.; Chen, Y.; Pham, H.; Go, A.; Su, H. Y.; Hu, C.; Wen, L.; Husain, S. Z.; Sugar, C. A.; Roos, J.; Ramos, S.; Lugea, A.; Dunn, M.; Stauderman, K.; Pandol, S. J. The Orai Ca(2+) channel inhibitor CM4620 targets both parenchymal and immune cells to reduce inflammation in experimental acute pancreatitis. *J. Physiol.* **2019**, *597* (12), 3085–3105.

(16) Tian, C.; Du, L.; Zhou, Y.; Li, M. Store-operated CRAC channel inhibitors: opportunities and challenges. *Future Med. Chem.* **2016**, *8* (7), 817–832.

(17) Derler, I.; Schindl, R.; Fritsch, R.; Heftberger, P.; Riedl, M. C.; Begg, M.; House, D.; Romanin, C. The action of selective CRAC channel blockers is affected by the Orai pore geometry. *Cell Calcium* **2013**, *53* (2), 139–151.

(18) Zitt, C.; Strauss, B.; Schwarz, E. C.; Spaeth, N.; Rast, G.; Hatzelmann, A.; Hoth, M. Potent inhibition of Ca²⁺ release-activated Ca²⁺ channels and T-lymphocyte activation by the pyrazole derivative BTP2. *J. Biol. Chem.* **2004**, *279* (13), 12427–12437.

(19) Sachdeva, R.; Fleming, T.; Schumacher, D.; Homberg, S.; Stitz, K.; Mohr, F.; Wagner, A. H.; Tsvilovskyy, V.; Mathar, I.; Freichel, M. Methylglyoxal evokes acute Ca²⁺ transients in distinct cell types and increases agonist-evoked Ca²⁺ entry in endothelial cells via CRAC channels. *Cell Calcium* **2019**, *78*, 66–75.

(20) Beech, D. J. Orai1 calcium channels in the vasculature. *Pfluegers Arch.* **2012**, *463* (5), 635–647.

(21) Li, J.; McKeown, L.; Ojelabi, O.; Stacey, M.; Foster, R.; O'Regan, D.; Porter, K. E.; Beech, D. J. Nanomolar potency and selectivity of a Ca²⁺ release-activated Ca²⁺ channel inhibitor against store-operated Ca²⁺ entry and migration of vascular smooth muscle cells. *Br. J. Pharmacol.* **2011**, *164* (2), 382–393.

(22) Edwards, J. M.; Neeb, Z. P.; Alloosh, M. A.; Long, X.; Bratz, I. N.; Peller, C. R.; Byrd, J. P.; Kumar, S.; Obukhov, A. G.; Sturek, M. Exercise training decreases store-operated Ca²⁺ entry associated with metabolic syndrome and coronary atherosclerosis. *Cardiovasc. Res.* **2010**, *85* (3), 631–640.

(23) Li, J.; Cubbon, R. M.; Wilson, L. A.; Amer, M. S.; McKeown, L.; Hou, B.; Majeed, Y.; Tumova, S.; Seymour, V. A.; Taylor, H.; Stacey, M.; O'Regan, D.; Foster, R.; Porter, K. E.; Kearney, M. T.;

Beech, D. J. Orai1 and CRAC channel dependence of VEGF-activated Ca^{2+} entry and endothelial tube formation. *Circ. Res.* **2011**, *108* (10), 1190–1198.

(24) Nurbaeva, M. K.; Eckstein, M.; Concepcion, A. R.; Smith, C. E.; Srikanth, S.; Paine, M. L.; Gwack, Y.; Hubbard, M. J.; Feske, S.; Lacruz, R. S. Dental enamel cells express functional SOCE channels. *Sci. Rep.* **2015**, *5*, 15803.

(25) Rice, L. V.; Bax, H. J.; Russell, L. J.; Barrett, V. J.; Walton, S. E.; Deakin, A. M.; Thomson, S. A.; Lucas, F.; Solari, R.; House, D.; Begg, M. Characterization of selective Calcium-Release Activated Calcium channel blockers in mast cells and T-cells from human, rat, mouse and guinea-pig preparations. *Eur. J. Pharmacol.* **2013**, *704* (1–3), 49–57.

(26) He, L.; Zhang, Y.; Ma, G.; Tan, P.; Li, Z.; Zang, S.; Wu, X.; Jing, J.; Fang, S.; Zhou, L.; Wang, Y.; Huang, Y.; Hogan, P. G.; Han, G.; Zhou, Y. Near-infrared photoactivatable control of Ca^{2+} signaling and optogenetic immunomodulation. *eLife* **2015**, *4*, No. e10024.

(27) Ma, G.; Liu, J.; Ke, Y.; Liu, X.; Li, M.; Wang, F.; Han, G.; Huang, Y.; Wang, Y.; Zhou, Y. Optogenetic Control of Voltage-Gated Calcium Channels. *Angew. Chem., Int. Ed.* **2018**, *57* (24), 7019–7022.

(28) Kyung, T.; Lee, S.; Kim, J. E.; Cho, T.; Park, H.; Jeong, Y. M.; Kim, D.; Shin, A.; Kim, S.; Baek, J.; Kim, J.; Kim, N. Y.; Woo, D.; Chae, S.; Kim, C. H.; Shin, H. S.; Han, Y. M.; Kim, D.; Heo, W. D. Optogenetic control of endogenous Ca^{2+} channels in vivo. *Nat. Biotechnol.* **2015**, *33* (10), 1092–1096.

(29) Broichhagen, J.; Frank, J. A.; Trauner, D. A Roadmap to Success in Photopharmacology. *Acc. Chem. Res.* **2015**, *48* (7), 1947–1960.

(30) Lerch, M. M.; Hansen, M. J.; van Dam, G. M.; Szymanski, W.; Feringa, B. L. Emerging Targets in Photopharmacology. *Angew. Chem., Int. Ed.* **2016**, *55* (37), 10978–10999.

(31) Szymański, W.; Beierle, J. M.; Kistemaker, H. A. V.; Velema, W. A.; Feringa, B. L. Reversible photocontrol of biological systems by the incorporation of molecular photoswitches. *Chem. Rev.* **2013**, *113* (8), 6114–6178.

(32) Velema, W. A.; Szymanski, W.; Feringa, B. L. Photopharmacology: Beyond proof of principle. *J. Am. Chem. Soc.* **2014**, *136* (6), 2178–2191.

(33) Schonberger, M.; Althaus, M.; Fronius, M.; Clauss, W.; Trauner, D. Controlling epithelial sodium channels with light using photoswitchable amilorides. *Nat. Chem.* **2014**, *6* (8), 712–719.

(34) Broichhagen, J.; Schonberger, M.; Cork, S. C.; Frank, J. A.; Marchetti, P.; Bugliani, M.; Shapiro, A. M.; Trapp, S.; Rutter, G. A.; Hodson, D. J.; Trauner, D. Optical control of insulin release using a photoswitchable sulfonylurea. *Nat. Commun.* **2014**, *5*, 5116.

(35) Fehrentz, T.; Huber, F. M. E.; Hartrampf, N.; Bruegmann, T.; Frank, J. A.; Fine, N. H. F.; Malan, D.; Danzl, J. G.; Tikhonov, D. B.; Sumser, M.; Sasse, P.; Hodson, D. J.; Zhorov, B. S.; Klocker, N.; Trauner, D. Optical control of L-type Ca^{2+} channels using a diltiazem photoswitch. *Nat. Chem. Biol.* **2018**, *14* (8), 764–767.

(36) Hauwert, N. J.; Mocking, T. A. M.; Da Costa Pereira, D.; Kooistra, A. J.; Wijnen, L. M.; Vreeker, G. C. M.; Verweij, E. W. E.; De Boer, A. H.; Smit, M. J.; De Graaf, C.; Vischer, H. F.; de Esch, I. J. P.; Wijnmans, M.; Leurs, R. Synthesis and Characterization of a Bidirectional Photoswitchable Antagonist Toolbox for Real-Time GPCR Photopharmacology. *J. Am. Chem. Soc.* **2018**, *140* (12), 4232–4243.

(37) Hauwert, N. J.; Mocking, T. A. M.; Da Costa Pereira, D.; Lion, K.; Huppelschoten, Y.; Vischer, H. F.; De Esch, I. J. P.; Wijnmans, M.; Leurs, R. A Photoswitchable Agonist for the Histamine H3 Receptor, a Prototypic Family A G-Protein-Coupled Receptor. *Angew. Chem., Int. Ed.* **2019**, *58* (14), 4531–4535.

(38) Donthamsetti, P. C.; Broichhagen, J.; Vyklicky, V.; Stanley, C.; Fu, Z.; Visel, M.; Levitz, J. L.; Javitch, J. A.; Trauner, D.; Isacoff, E. Y. Genetically Targeted Optical Control of an Endogenous G Protein-Coupled Receptor. *J. Am. Chem. Soc.* **2019**, *141* (29), 11522–11530.

(39) Courtney, T. M.; Deiters, A. Enzyme Allostery: Now Controllable by Light. *Cell chemical biology.* **2019**, *26* (11), 1481–1483.

(40) Lubbe, A. S.; Liu, Q.; Smith, S. J.; de Vries, J. W.; Kistemaker, J. C. M.; de Vries, A. H.; Faustino, I.; Meng, Z.; Szymanski, W.; Herrmann, A.; Feringa, B. L. Photoswitching of DNA Hybridization Using a Molecular Motor. *J. Am. Chem. Soc.* **2018**, *140* (15), 5069–5076.

(41) Bléger, D.; Hecht, S. Visible-Light-Activated Molecular Switches. *Angew. Chem., Int. Ed.* **2015**, *54* (39), 11338–11349.

(42) Ma, G.; Wen, S.; He, L.; Huang, Y.; Wang, Y.; Zhou, Y. Optogenetic toolkit for precise control of calcium signaling. *Cell Calcium* **2017**, *64*, 36–46.

(43) Ishii, T.; Sato, K.; Kakumoto, T.; Miura, S.; Touhara, K.; Takeuchi, S.; Nakata, T. Light generation of intracellular Ca^{2+} signals by a genetically encoded protein BACCS. *Nat. Commun.* **2015**, *6*, 8021.

(44) Nguyen, N. T.; Ma, G.; Lin, E.; D'Souza, B.; Jing, J.; He, L.; Huang, Y.; Zhou, Y. CRAC channel-based optogenetics. *Cell Calcium* **2018**, *75*, 79–88.

(45) Morstein, J.; Awale, M.; Reymond, J. L.; Trauner, D. Mapping the Azolog Space Enables the Optical Control of New Biological Targets. *ACS Cent. Sci.* **2019**, *5* (4), 607–618.

(46) Knie, C.; Utecht, M.; Zhao, F.; Kulla, H.; Kovalenko, S.; Brouwer, A. M.; Saalfrank, P.; Hecht, S.; Blegler, D. ortho-Fluoroazobenzenes: visible light switches with very long-Lived Z isomers. *Chem. - Eur. J.* **2014**, *20* (50), 16492–16501.

(47) Maier, M. S.; Hull, K.; Reynders, M.; Matsuura, B. S.; Leippe, P.; Ko, T.; Schaffer, L.; Trauner, D. Oxidative Approach Enables Efficient Access to Cyclic Azobenzenes. *J. Am. Chem. Soc.* **2019**, *141* (43), 17295–17304.

(48) Ahmed, Z.; Siiskonen, A.; Virkki, M.; Priimagi, A. Controlling azobenzene photoswitching through combined ortho-fluorination and -amination. *Chem. Commun.* **2017**, *53* (93), 12520–12523.

(49) Suzuki, J.; Kanemaru, K.; Ishii, K.; Ohkura, M.; Okubo, Y.; Iino, M. Imaging intraorganellar Ca^{2+} at subcellular resolution using CEPIA. *Nat. Commun.* **2014**, *5*, 4153.

(50) Zhao, Y.; Araki, S.; Wu, J.; Teramoto, T.; Chang, Y.-F.; Nakano, M.; Abdelfattah, A. S.; Fujiwara, M.; Ishihara, T.; Nagai, T.; Campbell, R. E. An Expanded Palette of Genetically Encoded Ca^{2+} Indicators. *Science* **2011**, *333* (6051), 1888–1891.

(51) Zheng, S.; Ma, G.; He, L.; Zhang, T.; Li, J.; Yuan, X.; Nguyen, N. T.; Huang, Y.; Zhang, X.; Gao, P.; Nwokonko, R.; Gill, D. L.; Dong, H.; Zhou, Y.; Wang, Y. Identification of molecular determinants that govern distinct STIM2 activation dynamics. *PLoS Biol.* **2018**, *16* (11), No. e2006898.

(52) Tamplin, O. J.; Zon, L. I. Fishing at the cellular level. *Nat. Methods* **2010**, *7* (8), 600–601.

(53) Lin, H. F.; Traver, D.; Zhu, H.; Dooley, K.; Paw, B. H.; Zon, L. I.; Handin, R. I. Analysis of thrombocyte development in CD41-GFP transgenic zebrafish. *Blood* **2005**, *106* (12), 3803–3810.

(54) Beharry, A. A.; Woolley, G. A. Azobenzene photoswitches for biomolecules. *Chem. Soc. Rev.* **2011**, *40* (8), 4422–4437.

(55) Lerch, M. M.; Szymanski, W.; Feringa, B. L. The (photo)-chemistry of Stenhouse photoswitches: guiding principles and system design. *Chem. Soc. Rev.* **2018**, *47* (6), 1910–1937.

(56) Williams, A.; Gore, J.; Martin, P.; House, D. Pyrazole compounds acting against allergic, immune and inflammatory conditions. WO 2012/052458 A1, 2012.

(57) Calbo, J.; Weston, C. E.; White, A. J.; Rzepa, H. S.; Contreras-Garcia, J.; Fuchter, M. J. Tuning Azoheteroarene Photoswitch Performance through Heteroaryl Design. *J. Am. Chem. Soc.* **2017**, *139* (3), 1261–1274.

(58) Wei, M.; Zhou, Y.; Sun, A.; Ma, G.; He, L.; Zhou, L.; Zhang, S.; Liu, J.; Zhang, S. L.; Gill, D. L.; Wang, Y. Molecular mechanisms underlying inhibition of STIM1-Orai1-mediated Ca^{2+} entry induced by 2-aminoethoxydiphenyl borate. *Pflugers Arch.* **2016**, *468* (11–12), 2061–2074.

(59) Zheng, S.; Zhou, L.; Ma, G.; Zhang, T.; Liu, J.; Li, J.; Nguyen, N. T.; Zhang, X.; Li, W.; Nwokonko, R.; Zhou, Y.; Zhao, F.; Liu, J.; Huang, Y.; Gill, D. L.; Wang, Y. Calcium store refilling and STIM

activation in STIM- and Orai-deficient cell lines. *Pfluegers Arch.* **2018**, *470*, 1555–1567.

(60) Navarro-Borelly, L.; Somasundaram, A.; Yamashita, M.; Ren, D.; Miller, R. J.; Prakriya, M. STIM1-Orai1 interactions and Orai1 conformational changes revealed by live-cell FRET microscopy. *J. Physiol.* **2008**, *586* (Pt 22), 5383–401.

(61) McNally, B. A.; Somasundaram, A.; Yamashita, M.; Prakriya, M. Gated regulation of CRAC channel ion selectivity by STIM1. *Nature* **2012**, *482* (7384), 241–245.